# Investigation of microwave sintering of B-type carbonated hydroxyapatite bioceramics

Clémence Petit, Arnaud Le Tiec, Louis Pancrazi, Nathalie Douard

# Investigation of microwave sintering of B-type carbonated hydroxyapatite bioceramics

PETIT Clémence[1,a], LE TIEC Arnaud[1,2], Louis Pancrazi[1,2], DOUARD Nathalie[2,b*]

[1] Mines Saint-Etienne, Université Lyon, CNRS, UMR 5307 LGF, Centre SMS, F-42023 Saint-Etienne, France

[2] Mines Saint-Etienne, Université de Lyon, Université Jean Monnet, INSERM, U 1059 SAINBIOSE, 158, cours Fauriel, CS 62362 , 42023 Saint-Etienne Cedex 2, France

[a]clemence.petit@emse.fr, [b]douard@emse.fr

* Corresponding author: Nathalie Douard

**Keywords:** carbonated hydroxyapatite, microwave sintering, thermal stability, bioceramic

**Abstract.** B-type carbonated hydroxyapatite ($C_BHA$) is potentially an excellent biodegradable bioceramic for bone repair. However, conventional sintering results in formation of undesired phases. Therefore, microwave sintering of $C_BHA$ was investigated to assess the possibility to reduce formation of unwanted phases. Pellets with 0.8 mol% of B-type carbonate were sintered in a multimode instrumented cavity under static air with short thermal cycles. They were prepared from a $C_BHA$ powder alone and from a mixture of $C_BHA$ and carbon powder to generate a local *in-situ* $CO_2$ atmosphere. XRD, FT-IR, SEM and BET analyses indicated that $C_BHA$ densification with increase temperature lead to decomposition into apatite. The addition of carbon powder to the $C_BHA$ that generate a $CO_2$-rich atmosphere around the samples did not prevent the decomposition. Efficient control of temperature and atmosphere composition is required to improve microwave sintering of $C_BHA$ bioceramics.

## Introduction

To treat bone defect, calcium phosphate (CaP) bioceramics and especially hydroxyapatite (HA, $Ca_{10}(PO_4)_6(OH)_2$) represent a safe alternative to overcome the limitation of autologous graft (*e.g.*, donor site morbidity) and have been clinically implanted for more than 30 years [1]. Due to its chemical composition close to the mineral part of bone, macroporous HA is biocompatible, displays excellent osteoconductive feature and provides an intimate bone-material contact [2]. However, HA has a limited capacity to degrade [3,4] which can be associated with late deformity of the bone [5]. A solution to improve and tailor the biodegradation rate of HA would be to work on carbonated hydroxyapatite (CHA). CHA are biocompatible and their biodegradation rate, higher compared to HA, can be controlled *via* the quantity of carbonate ions content [4,6].

Carbonate ions can substitute either for $OH^-$ ions to form A-type CHA (noted $C_AHA$) or for $PO_4^{3-}$ ions to form B-type CHA ($C_BHA$) [7]. A-type carbonates ions are the result of a thermally activated reaction between the hydroxide ions of the apatite and a $CO_2$-rich atmosphere, which occurs mainly during sintering mostly performed, to date, through conventional (CV) sintering [8]. The biological evaluation of $C_AHA$ bioceramics showed either lower or, at best, equal biological response than HA in term of osteoblast adhesion and proliferation [9,10]. To our best knowledge, the improved biological properties of CHA are mostly attributed to B-type carbonate ions [11,12]. The B-type substitution, which is the preferential carbonate substitution found in the bone [13], is commonly obtained by wet precipitation at low temperature from solutions containing calcium, phosphate and carbonate ions [14,15]. To stabilize the resulting $C_BHA$ composition up to a temperature allowing its

sintering and avoid its decomposition, a sintering atmosphere rich in $CO_2$ is necessary [4,16–18]. Consequently, an enrichment of A-type carbonate ions occurs leading to the production of A/B-type CHA ceramic ($C_{A/B}HA$) [17,19]. Knowing that A-type carbonation had a detrimental effect on the densification of CHA [19], new sintering strategies allowing to limit or even to get rid of this A-type carbonation would be beneficial.

CV sintering (*i.e.*, resistive heating) requires long process time to achieve a homogeneous heat distribution. Performed under a $CO_2$-rich atmosphere, it results in excessive undesired A-type carbonate enrichment as well as grain growth [17,19]. Thus, the low thermal stability of $C_BHA$ prevents the production of ceramics free of A-type carbonate ions by CV sintering. Consequently, $C_{A/B}HA$ are obtained whose A-type carbonate content depends on the chemical composition of the initial powder (molar ratio of the B-type carbonates) and the sintering parameters (temperature and atmosphere).

On the contrary, during microwave (MW) sintering, heating of the material occurs by absorption of electromagnetic radiation, which depends on its own dielectric properties. Thanks to a volumetric heating with limited thermal gradients, MW sintering allows for shorter processing times [20–22]. It has been successfully used to sinter substituted CaP based materials [22–26]. The work of Kutty *et al.* demonstrated that HA is found to couple with MWs around 900 °C [27]. Their comparative study highlighted that HA ceramics with similar shrinkage are obtained with four times shorter processing time under MW than CV. To the best of our knowledge, no study deals with the MW sintering of CHA. Only the work of Li *et al.* [10,28] reported the preparation of $C_AHA$ under MWs by using a carbon precursor (SiC or activated carbon). Their method allowed to generate locally a $CO_2$ atmosphere enabling a carbonate for hydroxide substitution during heating.

This study aims to evaluate the feasibility of using MW to produce $C_BHA$. The work is based on the assumption that a rapid MW heating process would allow to get rid of a $CO_2$ rich atmosphere to sinter pure $C_BHA$. As such, sintering of $C_BHA$ pellets was investigated in a MW device working under static air atmosphere. The starting $C_BHA$ powder was used alone or mixed with a carbon precursor powder to generate locally a $CO_2$ atmosphere. Various thermal treatment conditions were used and the physico-chemical features of the resulting sintered samples were compared.

## Materials and methods

**Preparation of $C_BHA$ powder.** $C_BHA$ powder was synthesized by an aqueous precipitation method following the procedure detailed in [14]. Briefly, a diammonium hydrogen phosphate solution ($(NH_4)_2HPO_4$, 99 %, Merck, Germany) mixed with an ammonium hydrogen carbonate solution ($(NH_4)HCO_3$, 99 %, Merck, Germany) was added to a calcium nitrate solution ($Ca(NO_3)_2$, $4H_2O$, 99 %, Merck, Germany) maintained under stirring. Reagents ratios were calculated according to the following theoretical formula: $Ca_{9.2}(PO_4)_{5.2}(CO_3)_{0.8}(OH)_{1.2}$. The pH of the suspension was adjusted to 8.0 by the addition of 28 % ammonia solution (Merck, Germany) by means of a dosing pump (ProMinent, U.K.) coupled with a pH controller (Mettler Toledo M400, U.S.A.) and a pH electrode (Mettler Toledo Inpro 4800/120/PT100, U.S.A.). The temperature was regulated at 65 °C with an external T-probe connected to a cryothermostat (Huber, Germany). An argon flow (Air Products) was maintained in the reactors to prevent any atmospheric uncontrolled carbonation. After complete introduction of the phosphate and carbonate solution, the suspension was matured for 24 h and centrifuged at 4000 rpm for 5 min (ThermoFisher Scientific, France). The wet powder agglomerates obtained were dried, ground in absolute ethanol and sieved at 25 µm. The powder was finally heat treated at 550 °C for 10 h (Carbolite, United Kingdom) under air to remove the main synthesis residues. The resulting powder was hereafter denoted "$C_BHA$".

**Preparation of the $C_B$HA and carbon mixture.** The powder mixture was prepared by blending 90 wt.% of $C_B$HA powder with 10 wt.% of an amorphous carbon powder (Glassy carbon spherical powder 0.4 - 12 µm, Alfa Aesar, France). The powder mixture was desagglomerated and homogenized in absolute ethanol by ball-milling (VE, France) during 3 days with alumina balls in a powder / ball weight ratio of 0.1. After ball milling, the powder mixture was dried at 100 °C for 24 h. The resulting powder mixture was hereafter denoted "$C_B$HA-C".

**Pellets preparation.** The $C_B$HA and $C_B$HA-C powders were first uniaxially pressed at 60 MPa (Instron, USA) in a 13 mm diameter stainless steel die and then isostatically pressed (NV2-40-4E, Nova Swiss, Switzerland) at 300 MPa.

**The MW setup and sintering.** MW sintering experiments were carried out in an instrumented setup presented in Fig. 1 [29] working under static air and composed of a cavity (Fig. 1a) instrumented with a camera and a contactless temperature measurement (Fig. 1b). The multimode cuboid cavity (dimensions of 430 × 430 × 490 mm) is equipped with a magnetron powered by a 3 kW generator (*GMP30K, SAIREM, France*) working at a fixed frequency of 2.45 GHz. A mode stirrer made of copper blades is placed inside the cavity to obtain a homogeneous heating. The sample is inserted inside a sintering cell made of plates of aluminosilicate fibers (*KVS 184–400, RATH®, Germany*) as thermal insulator. This material meets the requirements of MW applications: transparency to MW, stability at high temperature (to 1800 °C) and low thermal conductivity (0.33 $W.m^{-1}.K^{-1}$ at 1400 °C). A SiC ring was used as a susceptor to initiate the sample's heating. A low lossy mullite tube (*C610, AMTS, France*) surrounded the sample to minimize the susceptor radiation to the sample at high temperature. Inside the cell, the sample's circular surface was placed on two alumina sample holders. The contactless measurement of temperature was set up with a bichromatic pyrometer sensitive to wavelengths 2-2.5 µm and working in the 250-1800 °C temperature range (Lumasense Technology, Germany). To obtain an accurate measurement, it is necessary to know the apparent emissivity ratio ($k = \varepsilon 1 / \varepsilon 2$) of the pellet in the experimental conditions. This ratio was determined with a calibration protocol detailed elsewhere [30,31]. Briefly, a small amount of a metallic powder with a known melting point was inserted in a hole at the pellet surface. The pellet was heated until the melting of the metal detected with a camera positioned outside the cavity (Fig. 1b). When the metal started to melt, the emissivity of the pyrometer was modified to match the pellet temperature with that of the metal melting temperature. In this study, germanium was used as the calibration metallic material according to its melting temperature (938 °C) matching the sintering temperature of $C_B$HA.

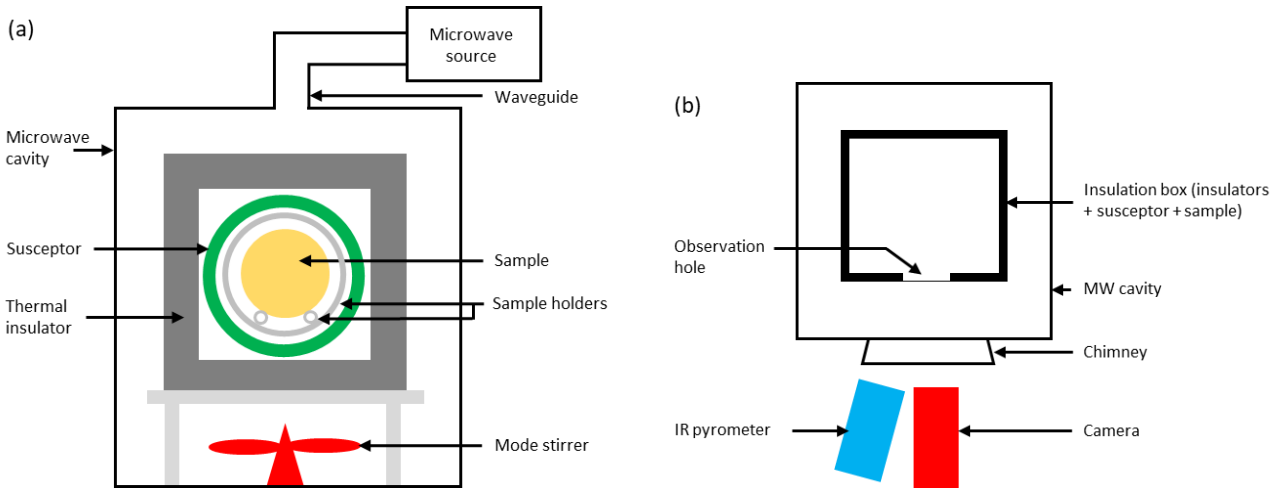


**Figure 1**: Scheme of the microwave setup: (a) front view and (b) top view

The thermal cycle was controlled by a specific homemade LabVIEW software. It used a PID controller based on the temperature measured by the pyrometer. The incident power delivered by the generator was continuously adjusted during the sintering cycle to match the measured temperature with the set temperature. The $C_B$HA and $C_B$HA-C pellets were sintered with different thermal cycles presented in Table 1. In the Table and hereafter, the samples are denoted according to nature of the starting powder used to prepare the pellets and the sintering cycle. The sintering cycle included the temperature of sintering, the heating rate where L stands for the lowest heating rate (30 °C/min) and H for the highest one (60 °C/min) followed by the holding time in minutes. After the holding time at the maximum temperature, the MW power was turned off and the samples were naturally cooled.

**Table 1.** Thermal cycles applied to $C_B$HA and $C_B$HA-C pellets

| Sample name | Sintering parameters | | | Time of thermal cycle* [min] |
|---|---|---|---|---|
| | Temperature [°C] | Heating rate [°C/min] | Holding time [min] | |
| $C_B$HA-900-L10 | 900 | 30 | 10 | 98 |
| $C_B$HA-900-H10 | 900 | 60 | 10 | 25 |
| $C_B$HA-900-H60 | 900 | 60 | 60 | 75 |
| $C_B$HA-1000-L10 | 1000 | 30 | 10 | 108 |
| $C_B$HA-1000-H10 | 1000 | 60 | 10 | 26 |
| $C_B$HA-C-900-H60 | 900 | 60 | 60 | 75 |

** The values correspond to the time required to heat from room temperature to the end of the holding time.*

**Physico-chemical characterization.** Crystalline phases were identified by means of a D8-A25 θ/θ X-ray diffractometer (Brüker, Germany) equipped with a Lynx-Eye Position Sensitive Detector (aperture angle, 2.946 °) using CuKα radiation and operating at 40 kV and 40 mA. X-ray diffraction (XRD) patterns were collected over a 2θ range of 10 – 40 ° with angle and time increments of 0.01 ° and 0.2 s, respectively. The experimental patterns were compared with the following reference patterns in ICDD-PDF (International Centre for Diffraction Data – Powder Diffraction Files): 00-009-0432 for HA, 00-037-1497 for CaO and 00-005-0586 for $CaCO_3$.
Fourier transform infrared (FTIR) absorption spectra were recorded using a MIR VERTEX 70 spectrometer (Bruker, Germany) equipped with a monolithic diamond ATR crystal (Quest ATR diamond, Specac, USA). IR spectra were recorded over the range of 4000 – 400 $cm^{-1}$ with a resolution of 2 $cm^{-1}$ and were obtained by averaging the signals obtained from 64 scans. The spectra were normalized with respect to the $\upsilon_4$ band of the $PO_4$ group at 600 $cm^{-1}$, according to a classical procedure [13] relevant for samples with similar B-site compositions.

**Thermal analysis.** The thermal behavior of the powder was characterized by thermogravimetric (TG) analysis (TGA/DSC instrument, Mettler Toledo) coupled with mass spectrometer (HPR 20, Hiden). Analysis were performed under air flow at 20 mL/min from ambient to 1200 °C with a heating rate of 20 °C/min. The emission of masses 12 and 44, corresponding to carbon and carbon dioxide respectively, were monitored during the thermal treatment.

**Microstructural analysis.** The specific surface area of sample was measured in triplicate using the Brunauer-Emmett-Teller (BET) 5-point method using a $N_2$ adsorption isotherm (ASAP 2010, Micromeritics, Germany) after outgassing the powder at 200 °C for 5 h. The microstructure of the sample was observed by scanning electron microscopy (SEM, JEOL 6500 F, USA) at 15 kV after gold coating (Q150R ES, Quorum Technologies). For powders, a sample was first dispersed by sonication for 5 min in absolute ethanol. The density of the sintered material was determined by the Archimedean method using distilled water as the liquid medium. Theoretical density (TD) value for $C_B$-HA with 0.8 mol of carbonate per mol of apatite was calculated at 3 $g.cm^{-3}$ [14].

## Results and discussion

**Characterization of the starting powders.** The XRD pattern of the $C_B$HA powder showed a poor crystalline structure (Fig. 2a). All the XRD peaks corresponded to the ICDD-PDF 009-0432 phase of HA. The XRD pattern of the carbon powder exhibited a broad C (002) diffraction peak in the range of 2θ between 20 ° and 30 ° attributed to the amorphous carbon structure, as well as crystalline peaks at 22.6 ° and 34.2 ° due to impurities [32,33].

Fig. 2b displays the IR spectrum of $C_B$HA powder. IR bands specific to $PO_4^{3-}$ group in the $\upsilon_2$ (470 $cm^{-1}$), $\upsilon_4$ (560 and 599 $cm^{-1}$), $\upsilon_1$ (962 $cm^{-1}$) and $\upsilon_3$ (1022 and 1090 $cm^{-1}$) were visible as well as IR bands attributed to OH groups at 627 $cm^{-1}$ ($\upsilon_L$) and 3572 $cm^{-1}$ ($\upsilon_S$). Additional bands attributed to the presence of carbonate in the HA lattice were visible. The ones at 1467, 1416 and 873 $cm^{-1}$ were attributed to B-type carbonate whereas the slight one visible at 879 $cm^{-1}$ was characteristic of A-type carbonate [8,13,17,34,35]. The assignation of the intense band at 1456 $cm^{-1}$ can be the contribution of A or B-type carbonate according to the aforementioned studies. If the presence of A-type carbonate had been significant, additional sharp bands would have been detected around 1545 and 1535 $cm^{-1}$. The absence of such bands suggested that the presence of A-type carbonate was weak in $C_B$HA powder and that the contribution detected at 1456 $cm^{-1}$ was mainly due to B-type carbonate. No IR band characteristic of synthesis residues was observed (*e.g.*, NO at 822 $cm^{-1}$). Thus, the starting $C_B$HA powder was a monophasic poorly crystalline B-type carbonated hydroxyapatite slightly carbonated in A sites. The FTIR spectrum of carbon powder (data not shown) presented no sharp absorption bands confirming its amorphous nature.

SEM micrograph revealed that the $C_B$HA powder was composed of nano-metric aggregated particles (Fig. 3a). Specific surface area of this powder was measured at 44.7 $m^2.g^{-1}$. SEM image of the carbon powder clearly revealed that the powder is composed of spherical particles whose size is coherent with the particle size distribution provided by the supplier (*i.e.*, between 0.4 and 12 µm).

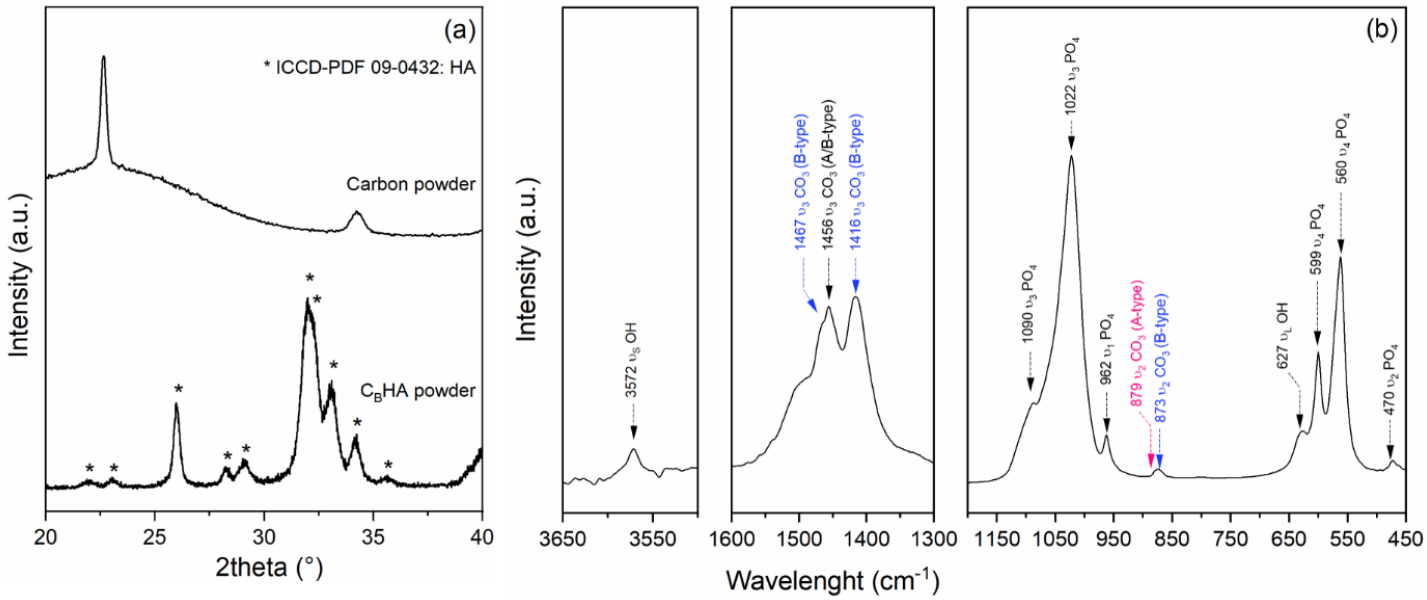


**Figure 2:** Physico-chemical analyses of the starting powder. (a) XRD pattern of $C_B$HA and carbon powders, (b) IR spectrum of $C_B$HA in the 3650-3500, 1600-1300 and 1200-450 $cm^{-1}$ range.

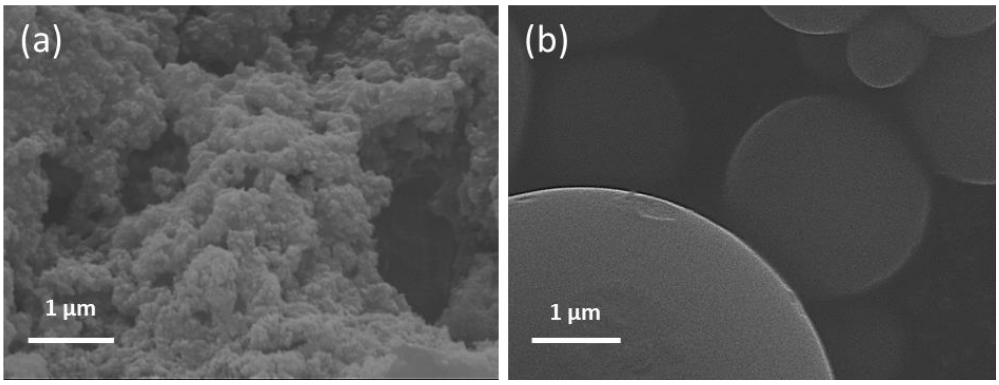


**Figure 3**: Microstructures of the starting powders. SEM micrographs of (a) the $C_B$HA powder with x 20 000 magnification and (b) the carbon powder with x 9000 magnification

**MW sintering of $C_B$HA under air.** After MW sintering of $C_B$HA pellets, the XRD patterns (Fig. 4a) revealed highly crystalline structures and exhibited the peaks of the HA phase (non-indexed peaks in the patterns) whatever the thermal cycle (Table 1). However, additional phases were identified in four sintered samples: $CaCO_3$ in $C_B$HA-900-H60 and CaO in $C_B$HA-1000-H10 and L10 as well as in $C_B$HA-900-L10. Only the shortest thermal treatment at the lowest temperature (*i.e.*, $C_B$HA-900-H10) resulted in a monophasic apatite without secondary phase detectable in XRD.

The FTIR spectra (Fig. 4b) presented the characteristic patterns of carbonated HA. Regardless of the thermal cycle, similar bands typical of the phosphate and hydroxide groups were observed in the MW sintered $C_B$HA compared to untreated $C_B$HA (Fig. 2a). As for the $C_B$HA powder, bands at 1467, 1456, 1416 and 873 $cm^{-1}$ indicated the presence of B-type carbonates. Additional B-type carbonate bands were observed after MW sintering under air at 1409 and 669 $cm^{-1}$. The presence of a slight amount of A-type carbonate was still detected at 879 $cm^{-1}$.

Table 2 presented the densities and relative densities of the sintered $C_B$HA pellets. The three samples sintered at 900 °C reached low final densities (relative densities in the range 71 – 71.5 %). Increasing the dwell time from 10 to 60 minutes did not significantly improved the result. As expected, increasing the sintering temperature (*i.e.*, to 1000°C) led to higher densification.

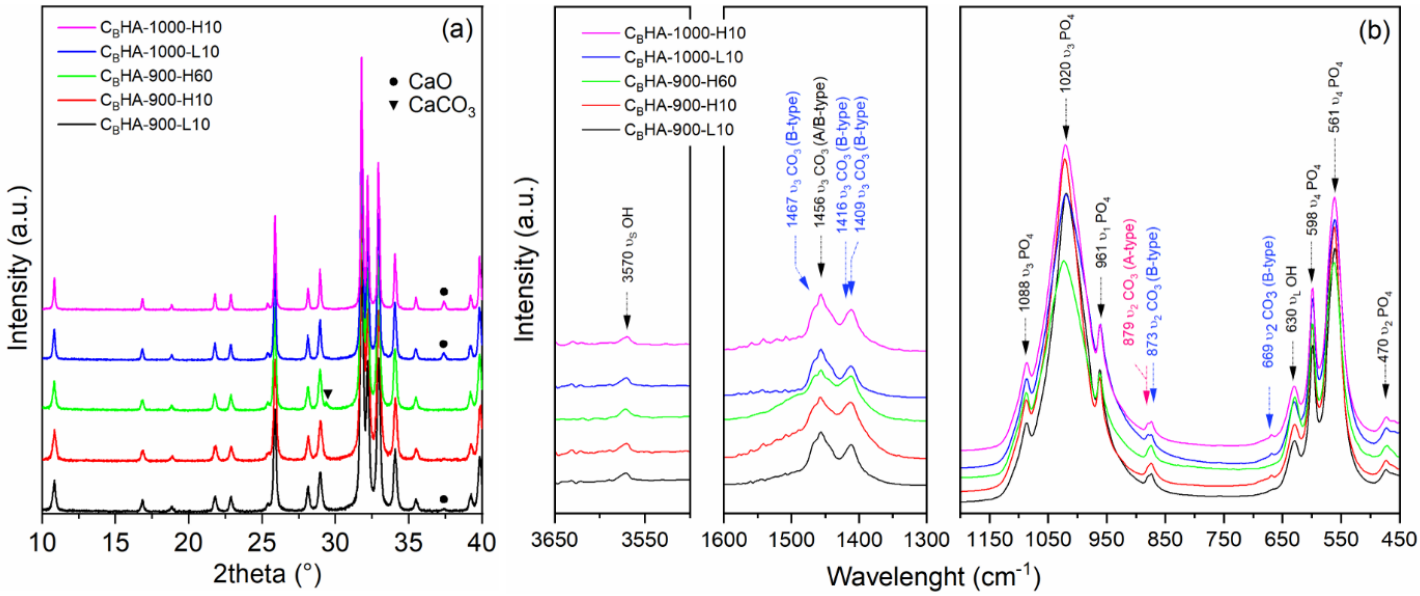


**Figure 4**: Physico-chemical characterization of the $C_B$HA sintered samples. (a) XRD patterns and (b) IR spectra in the 3650-3500, 1600-1300 and 1200-450 $cm^{-1}$ range

**Table 2.** Density and relative density of the sintered $C_B$HA pellets

| **Sample name** | **Density** [g.cm$^{-3}$] | **Relative density** [% TD] |
|---|---|---|
| $C_B$HA-900-L10 | 2.14 ± 0.07 | 71.3 ± 2.4 % |
| $C_B$HA-900-H10 | 2.13 ± 1.79 | 71.0 ± 1.8 % |
| $C_B$HA-900-H60 | 2.14 ± 0.02 | 71.5 ± 0.7 % |
| $C_B$HA-1000-L10 | 2.41 ± 0.06 | 80.2 ± 2.1 % |
| $C_B$HA-1000-H10 | 2.57 ± 0.07 | 85.7 ± 4.8 % |

Except for $C_B$HA-900-H10, the MW sintered pellets were biphasic crystalline products composed mainly of B-type carbonated HA coexisting with CaO or $CaCO_3$. The presence of CaO revealed by XRD is characteristic of the decarbonation of $C_B$HA described by Eq. 1 were x stands for the amount of B-type carbonate [36].

$$6\,Ca_{10-x}(PO_4)_{6-x}(CO_3)_xOH_{2-x}{}^{(s)} + 2x\,H_2O^{(g)} = (6-x)\,Ca_{10}(PO_4)_6OH_2{}^{(s)} + 4x\,CaO^{(s)} + 6x\,CO_2{}^{(g)}. \quad (1)$$

The $CaCO_3$ phase results from CaO carbonation according to Eq. 2.

$$CaO^{(s)} + CO_2{}^{(g)} = CaCO_3{}^{(s)}. \quad (2)$$

Regardless of the thermal cycle, heating at 1000 °C led to decomposition. At 900 °C, a high dwell time caused the decomposition of $C_B$HA and the carbonation of the resulting CaO phase whereas, rapid heating with short dwell time (*i.e.*, $C_B$HA-900-H10, Table 1) resulted in a monophasic apatite without secondary phase detectable in XRD. For comparison, during resistive thermal treatment with typical heating rate of 20 °C.min$^{-1}$, thermal decomposition of $C_B$HA began from about 600 °C [37]. The advantage of the MW technique lies mainly in the rapid heating of a sample. Here, this translates into a reduction of the time spent by the sample at high temperature allowing to avoid a deleterious reaction. On the contrary, such short thermal cycle led, in our condition, to poor densification. Full densification requires thermal cycles at higher temperatures and/or longer dwell time, which all lead to the $C_B$HA decomposition. These experiments revealed the need, even with MW, to sinter $C_B$HA under a $CO_2$ atmosphere to avoid its decomposition. The next section presents the results obtained with an *in-situ* $CO_2$ generation in the cavity during the thermal cycle.

**MW sintering of $C_B$HA-C under air.** To generate $CO_2$ under the MW cavity, the $C_B$HA powder was mixed with a carbon powder. Fig. 5 presents the results of the thermogravimetric (TG) analysis coupled with mass spectroscopy (MS) carried out on the $C_B$HA-C mixture. Three weight losses were detected in the TG signal. The first mass loss of 2.2 %, from room temperature to 500 °C, was attributed to the release of adsorbed species, such as water, ethanol or atmospheric $CO_2$. The second mass loss of approx. 12 %, in the range 500-800 °C, was associated to a high release of mass 12 and 44. It coincides well with the carbon content of the mixture (10 wt.%) and thus is mainly related to the decomposition of the carbon powder. The third mass loss of approx. 2.3 % appeared in the range 800-1000 °C and can be attributed to the loss of the B-type carbonates [38]. No significant mass loss was recorded above 1000 °C.

This analysis indicated that the carbon powder of the mixture is decomposed at 900 °C. Knowing that these data have been obtained under airflow, we hypothesised that carbon can be present in the form of $CO_2$ gas at 900 °C under static gas conditions. Thus, the following sintering experiment was performed at 900 °C on $C_B$HA-C pellets with the shortest thermal cycle (*i.e.* 60 °C/min with 60 min of holding time).

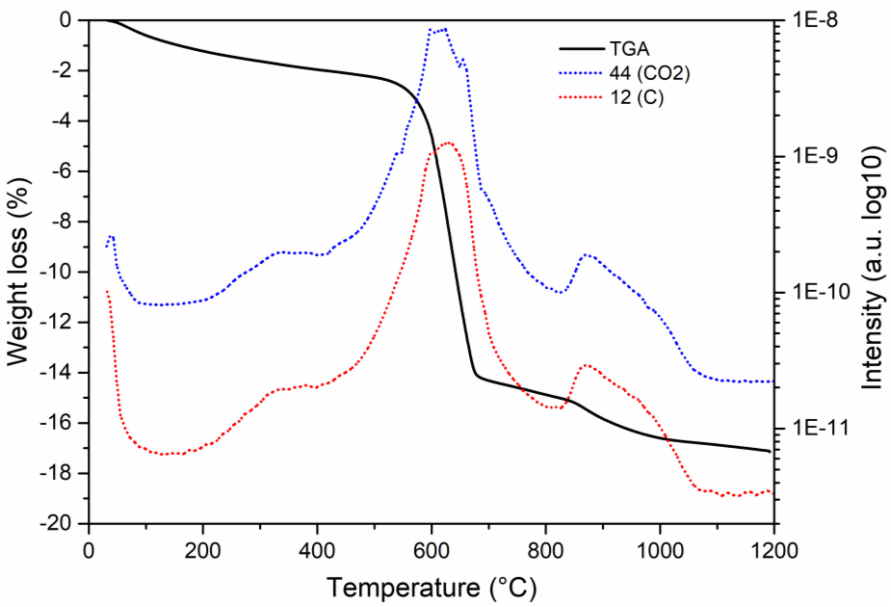


**Figure 5:** TG signal coupled to MS of the $C_B$HA-C powder mixture

The physico-chemical characterization of $C_B$HA-C-900-H60 is presented Fig. 6. The crystalline XRD pattern (Fig. 6a) still revealed the presence of secondary phases: $Ca(OH)_2$ and $CaCO_3$, both of them being characteristic of the decomposition of $C_B$HA. The $CaCO_3$ phase resulted from CaO reaction with ambient or *in situ* generated $CO_2$ according to Eq. 2 when $Ca(OH)_2$ phase comes from CaO hydration according to Eq. 3. The presence of $Ca(OH)_2$ is confirmed by FTIR analysis where an additional band is visible at 3642 $cm^{-1}$ (Fig. 6b).

$$CaO^{(s)} + H_2O^{(g)} = Ca(OH)_2{}^{(s)}. \quad (3)$$

**Figure 7**Fig. 7 showed the cross-section of the $C_B$HA-C pellet before and after sintering. The colour change (from greyish to white) after sintering inside the sample proves the total decomposition of the carbon powder during the thermal treatment. Unfortunately, the *in-situ* generated $CO_2$ in the MW cavity was insufficient to prevent decomposition of $C_B$HA at 900°C.

The SEM image of the surface of sintered pellet (Fig. 8a) shows spherical pores with a size in the range 1 - 10 µm. These pores, not present in the $C_B$HA samples (data not shown), resulted from the release of the carbon powder during its decomposition. At higher magnification (Fig. 8b), a residual micrometer-sized porosity left by incomplete sintering is visible.

The pores left by carbon powder decomposition is a new level of porosity, which is added to the porosity associated to the incomplete sintering. Thus, the relative density of $C_B$HA-C should be lower than the values for $C_B$HA for identical thermal cycles. However, the $C_B$HA-C-900-H60 sintered pellet has a relative density of 69.9 ± 1.1 %, which is very close to the value of the $C_B$HA-900-H60 pellet (71 %). Therefore, the $C_B$HA-C-900-H60 pellet probably densified better than the $C_B$HA pellets during sintering. This apparent inconsistency can be linked to the particularities of MW sintering and temperature measurement. During MW sintering, the ceramic materials heat thanks to direct interaction with electromagnetic field. The capability to heat of a ceramic is mainly related to the dielectric properties of the material itself [39]. In our case, it can be hypothesized that $C_B$HA and $C_B$HA-C samples interacted differently with MW due to the difference of dielectric properties between CHA and activated carbon, in spite of the small amount of carbon powder in the $C_B$HA-C pellet [27,40]. Moreover, measurement of temperature during MW sintering by pyrometers can also bring some inconsistencies. The pyrometer only measures the temperature at a spot on the sample's surface. Even if MW heating is mainly volumetric, the temperature measured by the pyrometer can

be lower than the real temperature at the core of the sample. Different authors already discussed this temperature gradient in MW-sintered porcelain samples ([41,42]). Moreover, an accurate temperature measurement by pyrometry needs a calibration procedure, *i.e.*, needs to measure the emissivity of the sample's surface in the cavity environment. A calibration procedure of emissivity based on the melting point of a metal was used in this study. This protocol allowed for an accurate temperature measurement during MW sintering of ceramics in previous studies ([30,43,44]). In our case, the presence of carbon in the $C_B$HA-C pellets could slightly change the emissivity of the surface, in spite of the low amount of carbon in the sample and its total decomposition at temperatures higher than 700°C. These different reasons can explain why $C_B$HA and $C_B$HA-C sintered samples exhibit different values of density.

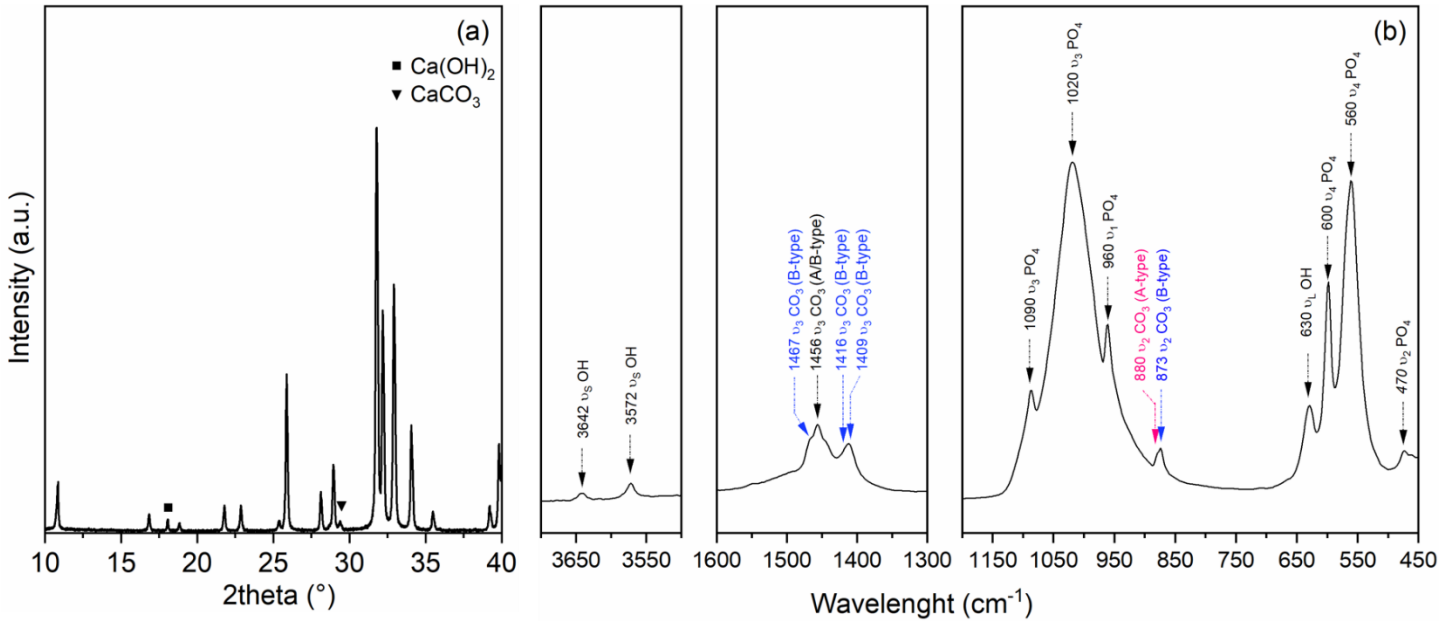


**Figure 6**: Physico-chemical characterization of the $C_B$HA-C-900-H60 sample. (a) XRD pattern, (b) FTIR spectrum and (c) magnified view of the FTIR spectrum

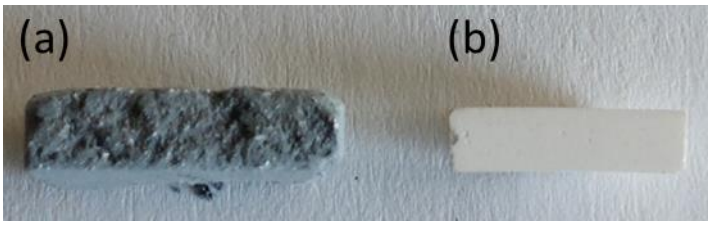


**Figure 7:** Cross-section of the $C_B$HA-C-900-H60 pellet (a) before and (b) after sintering

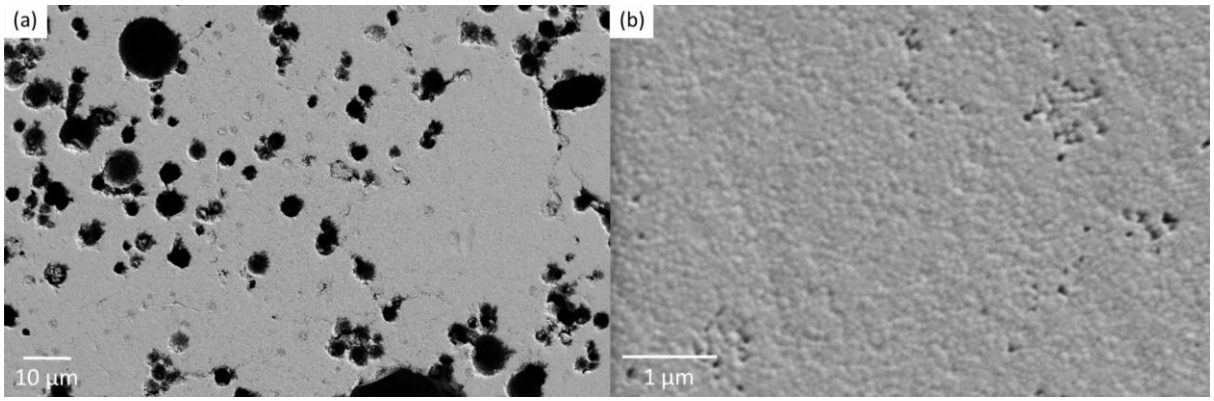

**Figure 8**: SEM images of the $C_B$HA-C-900-H60 at two magnifications: (a) x 2000 and (b) x 30000

## Conclusions

MW sintering of $C_B$HA samples were investigated under static air in two conditions: starting from pure $C_B$HA and from $C_B$HA mixed with carbon to generate *in-situ* $CO_2$. A short thermal cycle (900°C, 60°C/min, 10 min) led to an apparent monophasic $C_B$HA but did not achieve a high final density. A higher temperature increased the density but decomposition of apatitic phase occurred. The presence of carbon in the pellets effectively generated an *in situ* local $CO_2$ atmosphere but insufficient to avoid the decomposition of $C_B$HA. This preliminary investigation could be deepened to optimize the sintering conditions and the preparation of the powder mixtures. It points out as well the critical step of temperature measurement during MW sintering. Over a longer-term perspective, the development of a set-up to sinter $C_B$HA in MW cavity with a controlled $CO_2$ flow appears necessary.

## Acknowledgements

The authors want to acknowledge the support of David Marchat for powder synthesis, Christophe Meunier for MW sintering experiments, Marilyne Mondon for scanning electronic microscopy, Olivier Valfort for X-ray diffraction and Laetitia Vieille for thermogravimetric analyses.

## References

[1] V. Campana, G. Milano, E. Pagano, M. Barba, C. Cicione, G. Salonna, W. Lattanzi, G. Logroscino, Bone substitutes in orthopaedic surgery: from basic science to clinical practice, J. Mater. Sci. Mater. Med. 25 (2014) 2445–2461. https://doi.org/10.1007/s10856-014-5240-2.

[2] W. Habraken, P. Habibovic, M. Epple, M. Bohner, Calcium phosphates in biomedical applications: materials for the future?, Mater. Today. 19 (2016) 69–87. https://doi.org/10.1016/j.mattod.2015.10.008.

[3] R. Detsch, H. Mayr, G. Ziegler, Formation of osteoclast-like cells on HA and TCP ceramics, Acta Biomater. 4 (2008) 139–148. https://doi.org/10.1016/j.actbio.2007.03.014.

[4] J. Barralet, M. Akao, H. Aoki, H. Aoki, Dissolution of dense carbonate apatite subcutaneously implanted in Wistar rats, J. Biomed. Mater. Res. 49 (2000) 176–182. https://doi.org/10.1002/(SICI)1097-4636(200002)49:2<176::AID-JBM4>3.0.CO;2-8.

[5] A. Ogose, T. Hotta, H. Kawashima, N. Kondo, W. Gu, T. Kamura, N. Endo, Comparison of hydroxyapatite and beta tricalcium phosphate as bone substitutes after excision of bone tumors, J. Biomed. Mater. Res. B Appl. Biomater. 72 (2005) 94–101. https://doi.org/10.1002/jbm.b.30136.

[6] G. Spence, N. Patel, R. Brooks, W. Bonfield, N. Rushton, Osteoclastogenesis on hydroxyapatite ceramics: the effect of carbonate substitution, J. Biomed. Mater. Res. A. 92 (2010) 1292–1300. https://doi.org/10.1002/jbm.a.32373.

[7] R.Z. LeGeros, O.R. Trautz, E. Klein, J.P. LeGeros, Two types of carbonate substitution in the apatite structure, Experientia. 25 (1969) 5–7. https://doi.org/10.1007/BF01903856.
[8] M.E. Fleet, Carbonated Hydroxyapatite: Materials, Synthesis, and Applications, Jenny Stanford Publishing, New York, 2014. https://doi.org/10.1201/b17954.
[9] S.A. Redey, M. Nardin, D. Bernache-Assolant, C. Rey, P. Delannoy, L. Sedel, P.J. Marie, Behavior of human osteoblastic cells on stoichiometric hydroxyapatite and type A carbonate apatite: role of surface energy, J. Biomed. Mater. Res. 50 (2000) 353–364. https://doi.org/10.1002/(sici)1097-4636(20000605)50:3<353::aid-jbm9>3.0.co;2-c.
[10] B. Li, X. Liao, L. Zheng, H. He, H. Wang, H. Fan, X. Zhang, Preparation and cellular response of porous A-type carbonated hydroxyapatite nanoceramics, Mater. Sci. Eng. C. 32 (2012) 929–936. https://doi.org/10.1016/j.msec.2012.02.014.
[11] L.T. Bang, S. Ramesh, J. Purbolaksono, Y.C. Ching, B.D. Long, H. Chandran, S. Ramesh, R. Othman, Effects of silicate and carbonate substitution on the properties of hydroxyapatite prepared by aqueous co-precipitation method, Mater. Des. 87 (2015) 788–796. https://doi.org/10.1016/j.matdes.2015.08.069.
[12] R.Z. LeGeros, R.Z. LeGeros, Calcium phosphates in oral biology and medicine, Karger, Basel, 1991.
[13] C. Rey, B. Collins, T. Goehl, I.R. Dickson, M.J. Glimcher, The carbonate environment in bone mineral: A resolution-enhanced fourier transform infrared spectroscopy study, Calcif. Tissue Int. 45 (1989) 157–164. https://doi.org/10.1007/BF02556059.
[14] A. Boyer, D. Marchat, D. Bernache-Assollant, Synthesis and Characterization of Cx-Siy-HA for Bone Tissue Engineering Application, Key Eng. Mater. (2013). https://doi.org/10.4028/www.scientific.net/KEM.529-530.100.
[15] N. Douard, L. Leclerc, G. Sarry, V. Bin, D. Marchat, V. Forest, J. Pourchez, Impact of the chemical composition of poly-substituted hydroxyapatite particles on the in vitro pro-inflammatory response of macrophages, Biomed. Microdevices. 18 (2016) 27. https://doi.org/10.1007/s10544-016-0056-0.
[16] E. Landi, G. Celotti, G. Logroscino, A. Tampieri, Carbonated hydroxyapatite as bone substitute, J. Eur. Ceram. Soc. 23 (2003) 2931–2937. https://doi.org/10.1016/S0955-2219(03)00304-2.
[17] J.P. Lafon, E. Champion, D. Bernache-Assollant, Processing of AB-type carbonated hydroxyapatite Ca10−x(PO4)6−x(CO3)x(OH)2−x−2y(CO3)y ceramics with controlled composition, J. Eur. Ceram. Soc. 28 (2008) 139–147. https://doi.org/10.1016/j.jeurceramsoc.2007.06.009.
[18] M. Safarzadeh, C.F. Chee, S. Ramesh, M.N.A. Fauzi, Effect of sintering temperature on the morphology, crystallinity and mechanical properties of carbonated hydroxyapatite (CHA), Ceram. Int. 46 (2020) 26784–26789. https://doi.org/10.1016/j.ceramint.2020.07.153.
[19] Z. Zyman, M. Tkachenko, CO2 gas-activated sintering of carbonated hydroxyapatites, J. Eur. Ceram. Soc. 31 (2011) 241–248. https://doi.org/10.1016/j.jeurceramsoc.2010.09.005.
[20] D.K. Agrawal, Microwave processing of ceramics, Curr. Opin. Solid State Mater. Sci. 3 (1998) 480–485. https://doi.org/10.1016/S1359-0286(98)80011-9.
[21] M. Oghbaei, O. Mirzaee, Microwave versus conventional sintering: A review of fundamentals, advantages and applications, J. Alloys Compd. 494 (2010) 175–189. https://doi.org/10.1016/j.jallcom.2010.01.068.
[22] P. Sikder, Y. Ren, S.B. Bhaduri, Microwave processing of calcium phosphate and magnesium phosphate based orthopedic bioceramics: A state-of-the-art review, Acta Biomater. 111 (2020) 29–53. https://doi.org/10.1016/j.actbio.2020.05.018.
[23] N. Somers, F. Jean, M. Lasgorceix, H. Curto, G. Urruth, A. Thuault, F. Petit, A. Leriche, Influence of dopants on thermal stability and densification of β-tricalcium phosphate powders, Open Ceram. 7 (2021) 100168. https://doi.org/10.1016/j.oceram.2021.100168.

[24] Y. Fang, D.K. Agrawal, D.M. Roy, R. Roy, Fabrication of porous hydroxyapatite ceramics by microwave processing, J. Mater. Res. 7 (1992) 490–494. https://doi.org/10.1557/JMR.1992.0490.
[25] Y. Fang, D.K. Agrawal, D.M. Roy, R. Roy, Microwave sintering of hydroxyapatite ceramics, J. Mater. Res. 9 (1994) 180–187. https://doi.org/10.1557/JMR.1994.0180.
[26] A. Chanda, S. Dasgupta, S. Bose, A. Bandyopadhyay, Microwave sintering of calcium phosphate ceramics, Mater. Sci. Eng. C. 29 (2009) 1144–1149. https://doi.org/10.1016/j.msec.2008.09.008.
[27] M.G. Kutty, S.B. Bhaduri, H. Zhou, A. Yaghoubi, In situ measurement of shrinkage and temperature profile in microwave- and conventionally-sintered hydroxyapatite bioceramic, Mater. Lett. 161 (2015) 375–378. https://doi.org/10.1016/j.matlet.2015.08.136.
[28] B. Li, X. Chen, B. Guo, X. Wang, H. Fan, X. Zhang, Fabrication and cellular biocompatibility of porous carbonated biphasic calcium phosphate ceramics with a nanostructure, Acta Biomater. 5 (2009) 134–143. https://doi.org/10.1016/j.actbio.2008.07.035.
[29] N. Khalile, C. Petit, C. Meunier, F. Valdivieso, Hybrid microwave sintering of alumina and 3 mol% Y2O3-stabilized zirconia in a multimode cavity – Influence of the sintering cell, Ceram. Int. (2022). https://doi.org/10.1016/j.ceramint.2022.03.072.
[30] R. Macaigne, S. Marinel, D. Goeuriot, C. Meunier, S. Saunier, G. Riquet, Microwave sintering of pure and TiO2 doped MgAl2O4 ceramic using calibrated, contactless in-situ dilatometry, Ceram. Int. 42 (2016) 16997–17003. https://doi.org/10.1016/j.ceramint.2016.07.206.
[31] J. Croquesel, D. Bouvard, J.-M. Chaix, C.P. Carry, S. Saunier, Development of an instrumented and automated single mode cavity for ceramic microwave sintering: Application to an alpha pure alumina powder, Mater. Des. 88 (2015) 98–105. https://doi.org/10.1016/j.matdes.2015.08.122.
[32] X.-Y. Liu, M. Huang, H.-L. Ma, Z.-Q. Zhang, J.-M. Gao, Y.-L. Zhu, X.-J. Han, X.-Y. Guo, Preparation of a Carbon-Based Solid Acid Catalyst by Sulfonating Activated Carbon in a Chemical Reduction Process, Molecules. 15 (2010) 7188–7196. https://doi.org/10.3390/molecules15107188.
[33] C.F. Ramirez-Gutierrez, R. Arias-Niquepa, J.J. Prías-Barragán, M.E. Rodriguez-Garcia, Study and identification of contaminant phases in commercial activated carbons, J. Environ. Chem. Eng. 8 (2020) 103636. https://doi.org/10.1016/j.jece.2019.103636.
[34] C. Rey, V. Renugopalakrishman, B. Collins, M.J. Glimcher, Fourier transform infrared spectroscopic study of the carbonate ions in bone mineral during aging, Calcif. Tissue Int. 49 (1991) 251–258. https://doi.org/10.1007/BF02556214.
[35] A. Paré, B. Charbonnier, P. Tournier, C. Vignes, J. Veziers, J. Lesoeur, B. Laure, H. Bertin, G. De Pinieux, G. Cherrier, J. Guicheux, O. Gauthier, P. Corre, D. Marchat, P. Weiss, Tailored Three-Dimensionally Printed Triply Periodic Calcium Phosphate Implants: A Preclinical Study for Craniofacial Bone Repair, ACS Biomater. Sci. Eng. 6 (2020) 553–563. https://doi.org/10.1021/acsbiomaterials.9b01241.
[36] J.-C. Labarthe, G. Bonel, G. Montel, Sur la structure et les propriétés des apatites carbonatées de type B phospho-calciques., Ann. Chim. 8 (1973) 289–301.
[37] J.P. Lafon, E. Champion, D. Bernache-Assollant, R. Gibert, A.M. Danna, Termal decomposition of carbonated calcium phosphate apatites, J. Therm. Anal. Calorim. 72 (2003) 1127–1134. https://doi.org/10.1023/A:1025036214044.
[38] A. Boyer, Synthèse, caractérisation et évaluation biologique d'apatites phosphocalciques carbo silicatées, thesis, Saint-Etienne, EMSE, 2014. http://www.theses.fr/2014EMSE0739 (accessed March 16, 2020).
[39] R.R. Mishra, A.K. Sharma, Microwave–material interaction phenomena: Heating mechanisms, challenges and opportunities in material processing, Compos. Part Appl. Sci. Manuf. 81 (2016) 78–97. https://doi.org/10.1016/j.compositesa.2015.10.035.

[40] J.A. Menéndez, A. Arenillas, B. Fidalgo, Y. Fernández, L. Zubizarreta, E.G. Calvo, J.M. Bermúdez, Microwave heating processes involving carbon materials, Fuel Process. Technol. 91 (2010) 1–8. https://doi.org/10.1016/j.fuproc.2009.08.021.
[41] W. Lerdprom, E. Zapata-Solvas, D.D. Jayaseelan, A. Borrell, M.D. Salvador, W.E. Lee, Impact of microwave processing on porcelain microstructure, Ceram. Int. 43 (2017) 13765–13771. https://doi.org/10.1016/j.ceramint.2017.07.090.
[42] T. Santos, L. Hennetier, V.A.F. Costa, L.C. Costa, Microwave versus conventional porcelain firing: Temperature measurement, J. Manuf. Process. 41 (2019) 92–100. https://doi.org/10.1016/j.jmapro.2019.03.038.
[43] D. Żymełka, S. Saunier, J. Molimard, D. Goeuriot, Contactless Monitoring of Shrinkage and Temperature Distribution during Hybrid Microwave Sintering, Adv. Eng. Mater. 13 (2011) 901–905. https://doi.org/10.1002/adem.201000354.
[44] F. Zuo, S. Saunier, S. Marinel, P. Chanin-Lambert, N. Peillon, D. Goeuriot, Investigation of the mechanism(s) controlling microwave sintering of α-alumina: Influence of the powder parameters on the grain growth, thermodynamics and densification kinetics, J. Eur. Ceram. Soc. 35 (2015) 959–970. https://doi.org/10.1016/j.jeurceramsoc.2014.10.025.